Photoluminescence-based spatially resolved temperature coefficient maps of silicon wafers and solar cells

Shuai Nie[1], Sissel Tind Kristensen[2], Alexander Gu[1], Robert Lee Chin[1], Thorsten Trupke[1], and Ziv Hameiri[1]

[1]University of New South Wales, Sydney, NSW, Australia
[2]University of Agder, Grimstad, Norway

Abstract — **In this paper, we present a method to obtain open circuit voltage images of silicon wafers and cells at different temperatures. The proposed method is then demonstrated by investigating the temperature coefficients of various regions across multi-crystalline silicon wafers and cells from different heights of two bricks with different dislocation densities. Interestingly, both low and high temperature coefficients are found in dislocated regions on the wafers. A large spread of temperature coefficient is observed at regions with similar performance at 298 K. Reduced temperature sensitivity is found to be correlated with increasing brick height and is exhibited by both wafers and cells. This may indicate that cells made from the top of the brick, although having higher defect concentration, actually suffer relatively less degradation in performance at higher temperatures.**

F.I. Introduction

Multi-crystalline silicon (mc-Si) solar cells have dominated the photovoltaic (PV) market over the past decade [1]. Similar to other commercialised solar cells, mc-Si solar cells are tested and optimised under standard test conditions (STC): A standard solar spectrum AM 1.5G, an irradiance of 1000 W/m^2 and a temperature of 298 K [2]. However, in the field, solar cell operating temperatures often deviate significantly from STC [3]. In

order to allow PV users to accurately predict energy production and PV companies to optimise their cells for non-STC, temperature coefficients (TC), which quantify the impact of temperature on the electrical properties of the solar cells, are of particular importance.

It has long been known that temperature has a significant impact on the performance of silicon solar cells [4–12]. This is mainly due to the temperature dependence of the band-gap energy (E_g) [11]. Silicon features a reduction of E_g with increasing temperature, which causes an increased short-circuit current density (due to higher absorption) and a reduced open-circuit voltage V_{OC} [due to increasing intrinsic carrier concentration (n_i)] [5, 13]. Green stated that the electron-hole concentration product, which depends on the type and magnitude of the recombination processes, is the key parameter determining V_{OC}, and thus, the temperature dependence of silicon solar cells [7]. For silicon solar cells, the temperature sensitivity of the efficiency mainly arises from the variation of V_{OC} with temperature [7]; understanding the thermal behavior of V_{OC} is therefore of high importance.

The absolute TC of the V_{OC} can be expressed as [5]

$$\mathrm{TC}\,(V_{OC}) = \frac{dV_{OC}}{dT} = -\frac{\frac{E_{g0}}{q} - V_{OC} + \frac{\gamma kT}{q}}{T}, \tag{F.1}$$

where E_{g0} is the band gap energy of the semiconductor material extrapolated to 0 K, q is the elementary charge, k is the Boltzmann constant, T is the temperature, and γ represents the temperature dependences of several parameters determining the diode saturation current density J_0 [5, 12]. The parameter γ also contains information regarding the dominant recombination mechanisms in the material [12]. Eq. (F.1) predicts a reduction in the absolute temperature sensitivity of V_{OC} with increasing V_{OC}. Moreover, it predicts an approximately linear reduction of V_{OC} with increasing temperature over a limited temperature range [7, 12].

The temperature dependence of solar cells is normally reported as an average value for the entire cell [4, 8, 9, 11, 14, 15]. This value is useful for the analysis of several factors that contribute to temperature dependence variations between different solar cells. For example, by combining experiment and simulation, Steinkemper *et al.* suggested that the temperature dependence of their investigated solar cells mainly originates from extrinsic recombination or surface recombination [11]. The study of Berthod *et al.* into TCs of compensated mc-Si solar cells identified variations in TCs for different cell positions along the bricks, with variations between aluminium back surface field (Al-BSF) and passivated emitter rear contact (PERC) cells due to differences in recombination mechanisms between the two cell structures [15].

There has been growing, but as-yet limited, research into the spatially resolved temperature dependence across wafers and solar cells [16–18]. Existing studies show a large

variation in the temperature sensitivity across wafers and cells. Eberle *et al.* have shown increased temperature sensitivity, particularly for V_{OC}, at cell areas with a high concentration of impurities, such as the edge of the cells [17]. More recently, Eberle *et al.* conducted an in-depth investigation into the local temperature-dependent behaviour of mc-Si wafers and cells [18]. They identified a reduction in temperature sensitivity of V_{OC} in regions containing dislocation clusters. The investigation into the potential causes highlights the involvement of impurities, potentially leading to Shockley-Read-Hall (SRH) recombination [19, 20], which leads to a decrease in the temperature sensitivity of the dislocated regions. These studies highlight the importance of conducting further spatial analysis into the temperature dependence of solar cells.

In this work, we investigate the temperature sensitivity of wafers and cells fabricated from several positions along two industrially grown *p*-type mc-Si bricks with different dislocation densities [21]. We used our recently developed spatially resolved photoluminescence (PL) based system to measure various regions such as grain boundaries, dislocation clusters and intra-grain regions. The results are correlated with the TCs of PERC cells fabricated using sister wafers in an industrial production line.

F.II. Experimental Method

A. Sample Preparation

Fourteen wafers from two industrially grown *p*-type boron-doped mc-Si centre bricks are used (produced in $\sim$2015), seven from each brick. Of the seven wafers obtained from each brick, two originate from near the top of the brick, two from near the bottom and the remaining three wafers from positions in between. One brick has a high dislocation density, while the second brick has a low dislocation density. The exact dislocation density is determined using the algorithm implemented in our commercial PL imaging tool (BT Imaging, LIS-R3) [21]. The resistivity of the wafers varies between 1.5 and 2.2 Ω·cm. The wafers were saw-damage etched (final thickness: $185 \pm 10\,\mu$m) before undergoing a phosphorus-based gettering process [22, 23]. After etching off the diffused layer, the wafers were recleaned before undergoing silicon nitride (SiN_x) passivation (75 nm) using an industrial plasma-enhanced chemical vapour deposition system (MAiA, Meyer Burger) [24]. Please note that wafers were not fired or annealed. Fourteen solar cells made from sister wafers are also included in the study. The cells were fabricated in an industrial PERC production line [21].

The samples are studied using our recently developed temperature dependent PL imaging system described below. The PL images are acquired at temperatures from 298 K to 343 K under 0.5 Sun illumination (the highest light intensity that currently can

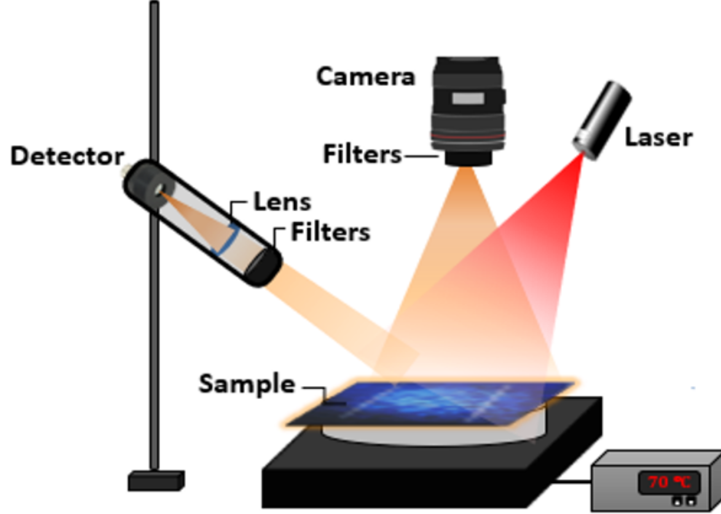

Figure F.1: Schematic of the experimental setup (not to scale).

be achieved for 6-inch samples with our setup). The relative PL images are then calibrated and converted into implied-V_{OC} (iV_{OC}) images using front detection quasi-steady-state (QSS) PL measurements (see below and in Refs. [25] and [26]) conducted under identical conditions to those used during the PL imaging. In order to test the validity of our method, the current-voltage (I-V) characteristics of the cells are measured at the same temperature range (298 K to 343 K) using a Wavelabs I-V tester (model SINUS-220).

B. Experimental Setup

Fig. F.1 shows a schematic of the PL-based measurement system used to obtain effective lifetime (τ_{eff}) and iV_{OC} images of wafers and cells at different temperatures. The system consists of a silicon charge-coupled device (CCD) camera and an 808 nm diode laser. Optical filters (long pass filters 950 nm and 850 nm, and a short pass filter 1000 nm) are placed in front of the camera to avoid detection of any reflected excitation light. A circular (diameter of 15 cm) temperature-controlled stage (Sinton Instruments WCT-120 TS) is used to heat the wafers and cells to higher temperatures [27]. The wafer temperatures are measured by a k-type thermocouple in direct contact with a similar sample.

The obtained PL images are then calibrated using the QSS-PL front detection method described in Refs. [25] and [26]. The PL emission from a selected region is focussed into a PL detector (InGaAs photodiode) with a lens. A customised filter set is attached to the lens to ensure the detection of only the band-to-band PL emission from the samples. A second photodiode is used to monitor the incident photon flux during measurements. Both photodiodes are connected to low-noise pre-amplifiers. In addition, a photoconductance (PC) signal from a defined region of the wafer is recorded by an inductive coil in the

Sinton WCT-120TS to improve the accuracy of the calibration procedure.

All signals are recorded with a data acquisition card that is connected to a computer. An additional flash is used when higher injection levels are required. The primary advantage of this setup is that it enables the determination of absolute τ_{eff} and iV_{OC} values for both metallised and non-metallised samples (in contrast to using only PC-based measurements [16, 27]). Moreover, this method is resilient to the effects of trapping and depletion region modulation (DRM) [28, 29].

C. Data Analysis Procedure

The conversion from relative PL counts to τ_{eff} and iV_{OC} maps is based on the relationship between the emitted PL intensity and the excess carrier density (Δn) at each pixel which is described by [30]:

$$\text{PL}_{xy}(T) = A_i(T)B(T)\left(N_{\text{dop}} + \Delta n_{xy}(T)\right)\Delta n_{xy}(T), \tag{F.2}$$

where PL_{xy} is the PL intensity at pixel (x, y), A_i is a calibration constant that depends on the specific sample and system [30]. A_i can be found either by matching the PC and PL measurement at high injection level (only for wafers) or using the self-consistent method (for both wafers and cells) [30, 31]. B is the radiative recombination coefficient [33, 34] and N_{dop} is the bulk dopant density.

In this study, the calibration of the constant A_i for PL imaging is performed using temperature-dependent QSS-PL measurements of τ_{eff} obtained from the illuminated surface of the sample. Using the determined A_i, $\tau_{\text{eff},xy}$ can be calculated using:

$$\tau_{\text{eff},xy}(T) = \frac{\left(-N_{\text{dop}} + \sqrt{{N_{\text{dop}}}^2 - 4\left(\frac{\text{PL}_{xy}(T)}{A_i(T)B(T)}\right)}\right)}{2G}, \tag{F.3}$$

where G is the generation rate considering the photon flux of the illumination source, the wafer reflectance and its thickness. $iV_{\text{OC},xy}$ is calculated using:

$$iV_{\text{OC},xy}(T) = \frac{kT}{q}\ln\left(\frac{\text{PL}_{xy}(T)}{A_i(T)B(T)n_i(T)^2}\right). \tag{F.4}$$

The band gap energy model of Passler [35] combined with the effective hole mass parameterisation of Couderc *et al.* [36] are used to determine n_i. The subsequent local absolute $\text{TC}(iV_{\text{OC},xy})$ is obtained from calibrated PL images taken at different temperatures via:

$$\text{TC}\left(iV_{\text{OC},xy}\right) = \frac{iV_{\text{OC},xy}\left(T_2\right) - iV_{\text{OC},xy}\left(T_1\right)}{T_2 - T_1}, \tag{F.5}$$

where T_1 is 298 K and T_2 is 343 K. Eq. (F.5) simplifies the determination of TC, as it uses only two temperatures. We have tested this simplification by taking six measurements

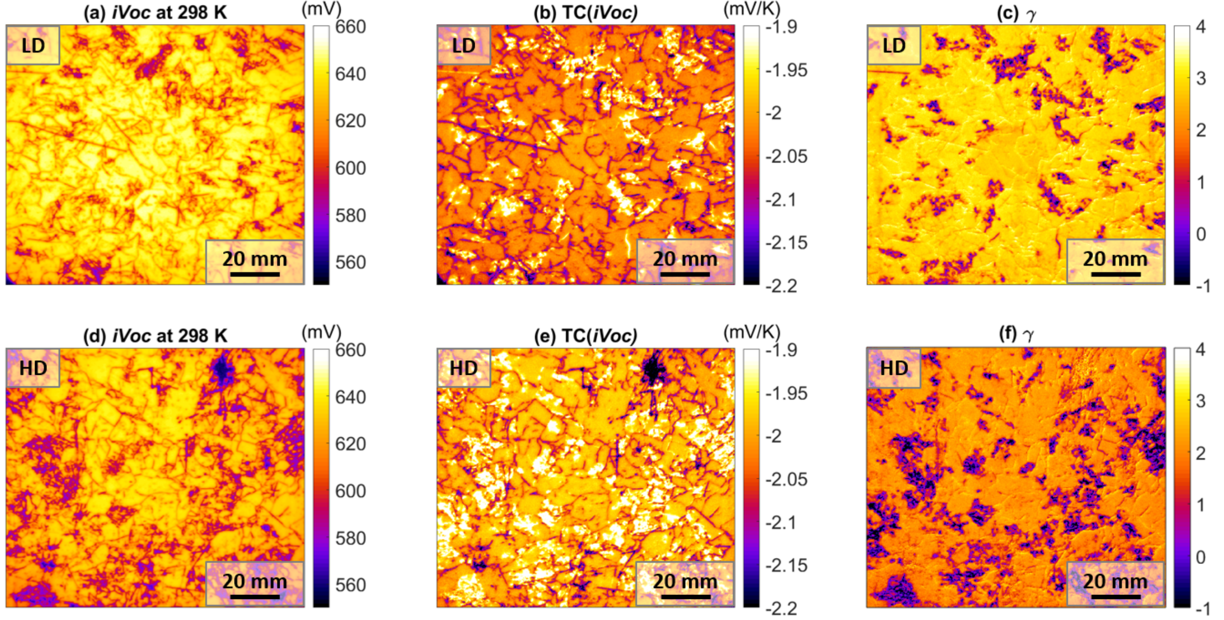

Figure F.2: Spatially resolved $iV_{\rm OC}$ at 298 K (a, d), TC($iV_{\rm OC}$) (b, e) and γ (c, f) of two wafers with low (a-c) and high (d-f) dislocation densities under 0.5 Sun illumination. Note that these images were cropped to present only the regions of interest.

between 298 K and 343 K at 10 K intervals. A linear reduction of $iV_{\rm OC}$ with increasing temperature is observed in this temperature range. A good agreement ($\sim 2\,\%$) is found between the comparison between the TC obtained from Eq. (F.5) and the TC obtained from the slope of the linear fit, thus confirming the validity of the simplified approach of Eq. (F.5).

F.III. Results and Discussion

A. Spatially Resolved Mapping

An example of the various parameter images obtained by the proposed method is depicted in Fig. F.2. Two wafers from the middle of each brick are compared [resistivity: $1.8 \pm 0.1\,\Omega$·cm; high and low dislocation densities]. Figs. F.2(a) and (d) show $iV_{\rm OC}$ maps at 298 K. As expected, lower $iV_{\rm OC}$ values are observed in areas with dislocation clusters (appear as dark clusters in the PL images) and grain boundaries (dark lines). The calculated average $iV_{\rm OC}$ of the highly dislocated (HD) wafer is 611 ± 3 mV, which is 15 mV ($\sim 2.5\,\%$) lower than the average $iV_{\rm OC}$ of the lowly dislocated (LD) wafer (626 ± 3 mV).

Images of TC($iV_{\rm OC}$) are displayed in Figs. F.2(b) and (e). A large variation of TC($iV_{\rm OC}$) across the wafers is observed. The data show that TC($iV_{\rm OC}$) is more negative in grain boundaries and some dislocation clusters, indicating a larger reduction of $iV_{\rm OC}$ with increasing temperature in these regions compared to other areas across the

Table F.1: Implied-V_{OC}, TC(implied-V_{OC}) of a highly dislocated cell from the middle of the brick.

PL-based	iV_{OC} at 298 K	TC(iV_{OC})
method	627 mV	-1.87 mV/K
I-V	V_{OC} at 298 K	TC(V_{OC})
measurement	625 mV	-1.89 mV/K

wafer. The majority of the dislocation clusters show lower temperature sensitivity. This observation contradicts the common belief that the temperature sensitivity is expected to increase with decreasing iV_{OC} [4, 12]. Previous studies have observed only low temperature sensitivity of dislocation clusters [17, 18]. However, in this study, dislocated regions of two tested bricks show both high and low temperature sensitivities. This discrepancy could possibly be explained by differences in the processing procedure for the investigated wafers.

Figs. F.2(c) and (f) present γ maps calculated by applying Eq. (F.1) to each pixel [17, 18]. There is a clear difference between the two bricks, with global values of 2.29 for the LD wafer and 1.35 for the HD wafer. Lower γ values (even negative), consequently reduced J_0 [17], are observed at dislocation clusters, explaining the more uniform γ distribution across the LD wafer (and larger average γ). The source for the interesting (and unexpected) negative γ is discussed in Refs. [14, 18, 37]. Dupré *et al.* explained that global negative γ values of cells are mostly due to an increase of external radiative efficiency (detailed explanation regarding external radiative efficiency can be found in Ref. [38]) at open circuit of these cells with temperature [14]. However, the physics behind this negative γ is still unclear and requires further investigation.

To assess the validity of our method, we compare cell measurements obtained using our proposed method with cell measurements obtained using the established *I-V* technique [15, 39–41]. Fig. F.3 illustrates the iV_{OC} map of one of the PERC cells originating from the middle of the HD brick [sister cell of the wafer of Figs. F.2(d)-(f)] and its corresponding TC(iV_{OC}) map under 0.5 Sun illumination. Note that a circular heat stage is used for the PL imaging, causing a circular pattern. Only the middle region is used for subsequent analysis. The local values are harmonically averaged and compared with the results obtained from global *I-V* measurements (using a Wavelab *I-V* tester) for the same solar cell. The harmonic average is used as it provides a better estimation of the material quality for predicting cell performance [42,43]. Table F.1 summarises the results. Excellent agreement with relative deviations in the range of 1 % is found between the two measurements.

By comparing iV_{OC} maps with TC(iV_{OC}) maps of the cells, the regions near the con-

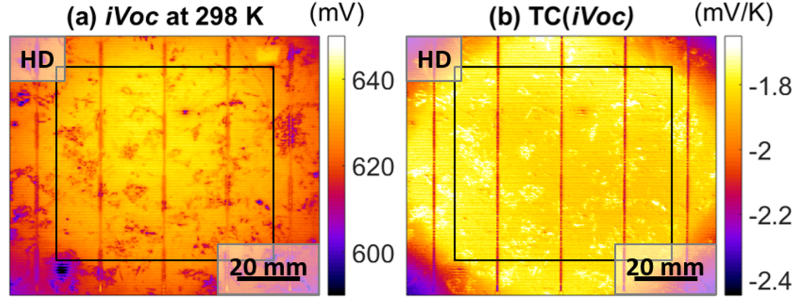

Figure F.3: (a) Spatially resolved iV_{OC} at 298 K and (b) TC(iV_{OC}) of a PERC cell originating from the middle of the highly dislocated brick under 0.5 Sun illumination.

tacts (especially busbars) show higher temperature sensitivity, as expected from the higher recombination in these areas in comparison with the well passivated regions between the contacts. Reduced temperature sensitivity regions are found to be correlated with dislocated areas. Comparing the cell with the wafer, the temperature sensitive regions across the sister wafer (such as grain boundaries and some dislocation clusters [Figs. F.2(d) and (e)]) are not as easily identified on the cell maps [Figs. F.3(a) and (b)]. The difference can be explained by the lateral conduction over the cell and the incomplete fabrication process of the wafers, particularly the lack of firing. This hypothesis requires further investigation and will be studied in our future work.

B. Impact of Brick Height

Fig. F.4(a) shows the harmonically averaged iV_{OC} at 298 K extracted from calibrated PL images of the wafers from both the HD and LD bricks. As expected, the LD brick has high iV_{OC} values compared to the HD brick. For both bricks, the highest iV_{OC} is observed in the middle of the brick; the iV_{OC} declines gradually towards the bottom and top of the brick. This trend follows the variation of material quality with brick height, where the top and bottom of the brick contains a higher impurities concentration due to segregation from the liquid-to-solid phase and diffusion from the crucible [44, 45]. A similar trend has been observed in Ref. [45]. The global V_{OC} values of the sister cells measured using a temperature dependent I-V tester are presented in Fig. F.4(b). The variation of V_{OC} along the brick is less obvious compared to the wafers, however, the V_{OC} of top and bottom cells are still lower than those of the more central cells. The cells exhibit higher voltage values compared to the sister wafers; this is more pronounced for bottom cells. This can be explained by the lack firing of the wafers, a process which often passivates large fractions of the grain boundaries [45].

Fig. F.4(c) shows the average TC(iV_{OC}) values extracted from calibrated PL images of the wafers and global TC(V_{OC}) values for the cells as a function of brick height. The

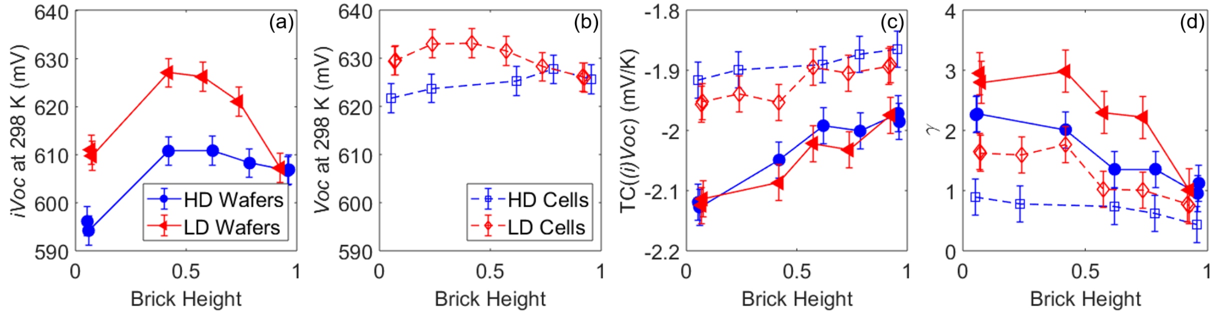

Figure F.4: Global results of wafers and sister cells with low and high dislocation densities as a function of brick height under 0.5 Sun illumination: (a) iV_{OC} at 298 K, (b) V_{OC} at 298 K, (c) TC(iV_{OC}) and TC(V_{OC}) and (d) γ.

TC(iV_{OC}) values of the investigated wafers are found to be less negative with increasing brick height (from -2.15 mV/K to -1.95 mV/K), although, the top wafers show reduced iV_{OC} values. The improved TCs of the top wafers can be explained by an increasing TC(τ_{eff}) towards the top of the brick, as discussed in Ref. [41]. Moreover, the increasing density of dislocation clusters showing low temperature sensitivity with increasing brick height (see Fig. F.7) could also contribute to the low temperature sensitivity towards top of the brick. This is likely due to increased concentration of impurities that causes low temperature sensitivity [18].

The cells exhibit a similar trend, with a lower temperature sensitivity and less variation along the brick. This is in agreement with previous studies presented in Refs. [15, 40, 41].

There is no clear difference (when considering the measurement uncertainty as represented by the error bars) in the global temperature sensitivity between the two bricks (for both wafers and cells). We cannot confidently pinpoint the impact of dislocation density on the global TC values since dislocation clusters show both high and low TC(iV_{OC}) as demonstrated in Fig. F.2.

Fig. F.4(d) shows the average γ values of the cells and wafers [calculated using Eq. (F.1)] as a function of brick height. Like the cells, the wafers exhibit a decreasing γ with increasing brick height. Berthod *et al.* observed a similar trend on compensated materials [15]. Interestingly, the wafers exhibit larger γ values compared to the cells and stronger variation along the brick, indicating a change of the limiting recombination mechanism from bottom to top of the brick.

Fig. F.5 shows the pixel-level TC(iV_{OC}) as a function of iV_{OC} at 298 K under 0.5 Sun illumination. The colour represents the data density normalised to unity ('1' represents the highest density). For all the measured wafers, as expected theoretically from Eq. (F.1), the temperature sensitivity tends to decrease with increasing iV_{OC}. However, it is very interesting to observe that regions with similar iV_{OC} (at 298 K) show a large spread, up

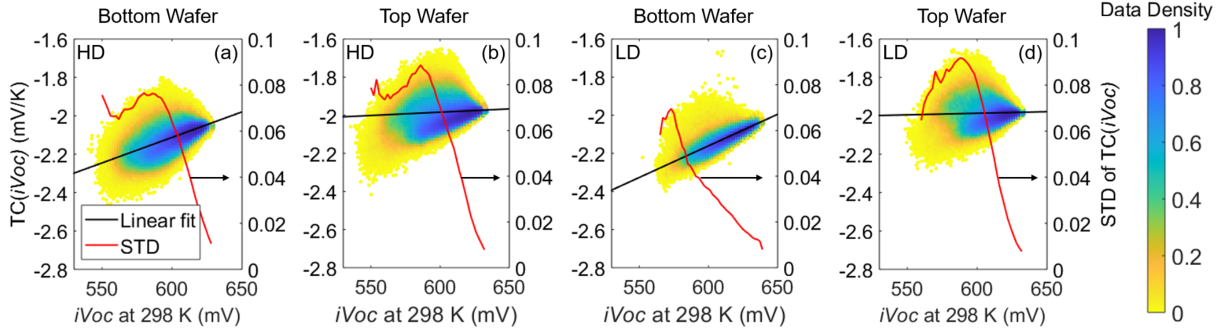

Figure F.5: Density scatter plot of TC(iV_{OC}) as a function of iV_{OC} at 298 K of highly dislocated wafers and lowly dislocated wafers from bottom and top of the bricks under 0.5 Sun illumination with the line of best linear fit (black) and TC(iV_{OC}) standard deviation (red) overlay. The standard deviation shown is for iV_{OC} bins of 2 mV.

to 40 %, in TC(iV_{OC}), showing that temperature sensitivity can only be well understood by spatially resolved measurements.

The spread of TC(iV_{OC}) across the wafers in the iV_{OC} domain is quantitatively determined as standard deviation (STD) of TC(iV_{OC}) at different iV_{OC} bins. For all wafers, low STD occurs at high iV_{OC}, while the medium to low iV_{OC} range shows high STD. A shift of TC(iV_{OC}) towards less negative values is noticeable for the top wafers. This is consistent with our observation that the average temperature sensitivity reduces with increasing brick height.

A linear fit of TC(iV_{OC}) as a function of iV_{OC} at 298 K is also included in Fig. F.5. A clear trend of reduced TC for increasing iV_{OC} is observed for the bottom wafers of both bricks. However, no clear trend can be observed for the top wafers due to the larger spread of TC across these wafers at medium to low iV_{OC} range (as indicated by the larger STD values).

The slope of the linear fit, representing the change of TC as a function of iV_{OC}, as a function of brick height is shown in Fig. F.6. It seems the slope of the fits decreases with increasing brick height, indicating a reduction in the TC variation across the wafers closer to the top of the brick. These results suggest that some disadvantages associated with mc-Si wafers originating from the top of the brick, such as a higher defect concentration resulting in lower performance at room temperature [44, 45], is weakened at higher temperatures.

Fig. F.7 presents maps of iV_{OC} at 298 K, TC(iV_{OC}), and the resulting γ of two wafers originating from the bottom (a-c) and top (d-f) of the HD brick. As expected, small grains and a large fraction of grain boundaries can be observed in the bottom wafer. It seems that for the bottom wafer, almost all the low-quality regions (grain boundaries and dislocated regions) show a higher temperature sensitivity compared to the intra-grain

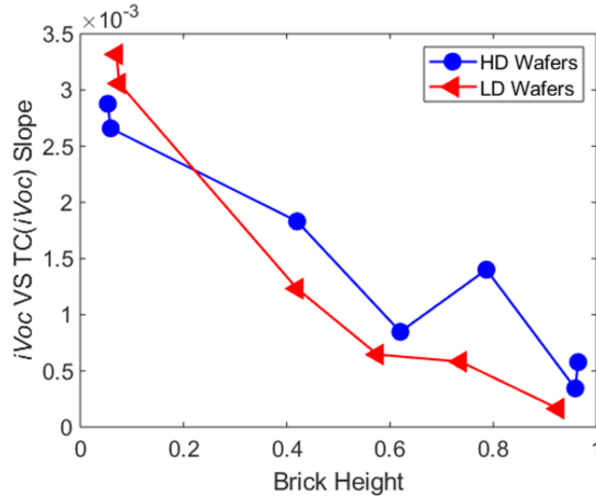

Figure F.6: Variation of TC with iV_{OC} at 298 K (slope of linear fit) as a function of brick height.

Table F.2: iV_{OC}, TC, and γ of different ROIs across a highly dislocated wafer from the top of the brick.

	iV_{OC} (mV)	TC(iV_{OC}) (mV/K)	γ
ROI (a)	584	-2.14	2.00
ROI (b)	580	-1.95	-0.32
ROI (c)	594	-1.95	0.19

regions. In contrast, the difference between these regions appears less significant in the top wafer, where most of the dislocation clusters show a low temperature sensitivity. In general, it seems that wafers from the top of the brick are less sensitive to temperature variations compared to wafers from the bottom (see global TC values in Fig. F.4). This could be attributed to the impact of a higher density of grain boundaries and different impurities in the lower wafer. It is also possible that the dislocations are decorated by different impurities with different impacts on the temperature sensitivity of the wafers. This will be discussed in the next section.

C. TC(iV_{OC}) of Dislocation Clusters

To investigate the source of the large variation in the TC(iV_{OC}) of dislocation clusters, dislocated areas with different TCs were selected for further investigation. Three different regions of interest (ROI) are defined [as shown in Figs. F.7(d) to (f)]. Table F.2 summarises the obtained parameters for these regions.

All three ROIs are low-quality regions containing dislocation clusters. ROIs (a) and (b) have a similar iV_{OC} at 298 K, but very different TC; whereas ROIs (b) and (c) have

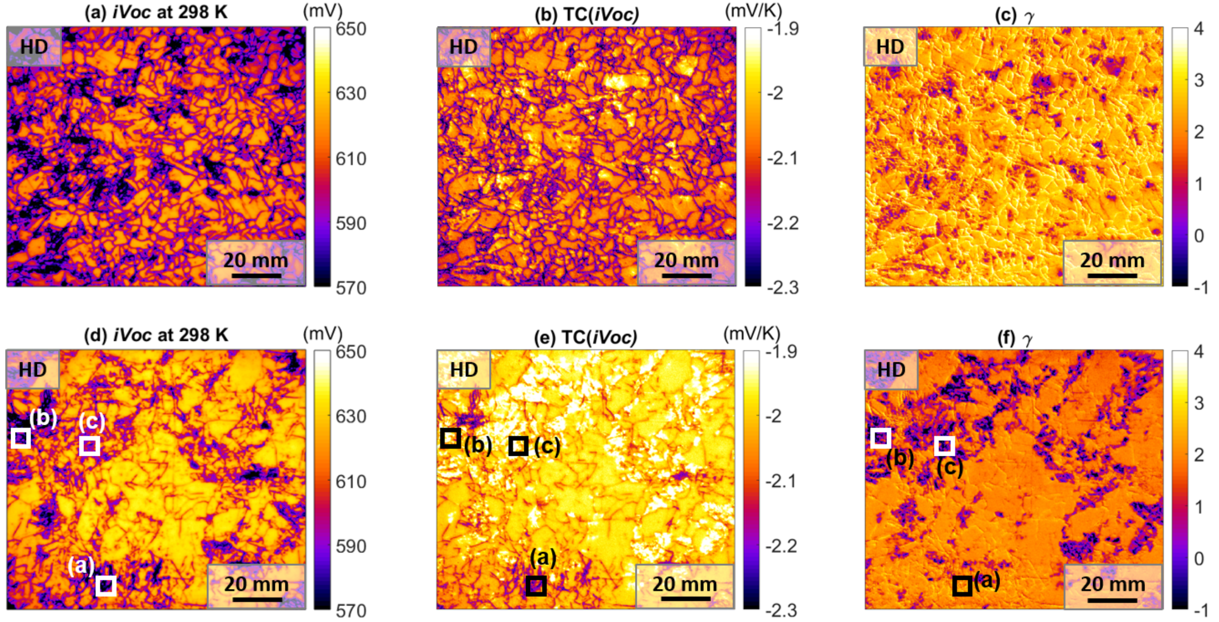

Figure F.7: Spatially resolved iV_{OC} at 298 K, TC (iV_{OC}) and γ of two highly dislocated wafers from the bottom (a-c) and the top (d-f) of the brick under 0.5 Sun illumination. Note that these images were cropped to present only the regions of interest. (The corresponding temperature-dependent τ_{eff} images are given in Appendix A).

a similar TC, but different iV_{OC}. The γ values of ROIs (b) and (c) are much smaller than one (and even negative), while for ROI (a) $\gamma = 2$, indicating that different dominant recombination mechanisms limit the performance of these three regions.

We examined these regions by micro-PL (μPL) spectroscopy [46]. Fig. F.8 shows the PL spectra of ROIs (a) and (c) at an actual sample temperature of 122 ± 7 K (the actual sample temperature is obtained by modelling the band to band (BB) peak [47]). Low temperatures are chosen for the investigation, as defect-peaks are strongly temperature-quenched and therefore more noticeable at lower temperatures. The four dislocation-related lines are labelled as D1 (0.812 eV), D2 (0.875 eV), D3 (0.934 eV), and D4 (1.000 eV) [48]. D1, D3 and D4 can be identified in both regions, indicating that both regions are highly dislocated.

To distinguish between these regions, temperature-dependent μ-PL measurements are performed at a wide temperature range from 127 K to 302 K. An example is shown in Fig. F.9 for ROI (c). The D1 peak is dominant at medium- to high-temperatures, while D3 and D4 cannot be observed above 240 K. Each defect peak is fitted using the Voigt function [49]. Since the D1 peak can be observed across the entire temperature range (even at high temperatures), we extract the activation energies (E_a) of D1-associated defects at both ROIs [50, 51] by using an Arrhenius plot (Fig. F.10) to fit the spectrally integrated defect PL.

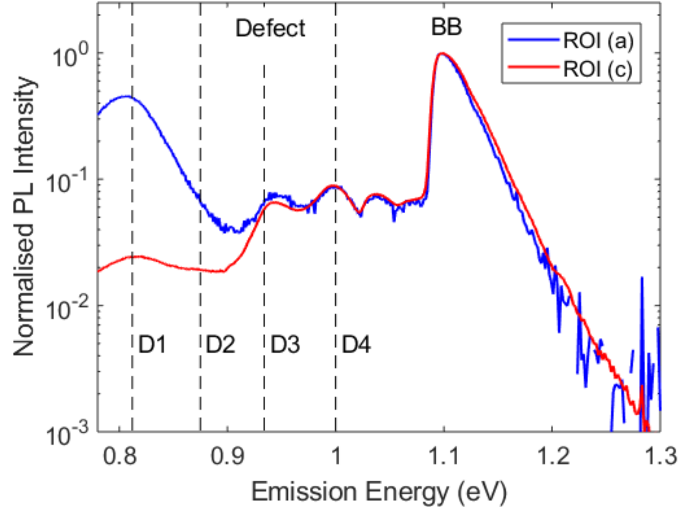

Figure F.8: PL spectra of ROIs (a) and (c) of a highly dislocated wafer from the top of the brick at 122 ± 7 K (actual sample temperature) under 20 Suns.

In order to extract E_{a} of the D1-associated defects, the spectrally integrated $\mathrm{PL}_{\mathrm{defect}}(T,\Delta n)$ is fitted to the equation below (the derivation of this equation is given in Appendix B) [52]:

$$\mathrm{PL}_{\mathrm{defect}}\,(T,\Delta n) = \frac{\mathrm{PL}_0}{1 + \frac{C}{\Delta n(T)} T^{1.5} \exp\left[-\frac{E_{\mathrm{a}}}{kT}\right]} \tag{F.6}$$

where PL_0 and C are positive constants. PL_0 represents the $\mathrm{PL}_{\mathrm{defect}}$ as the temperature approached 0 K. $\Delta n(T)$ is calculated relatively using the spectrally integrated BB PL and the ionised acceptors (N_A^-) [53] as $\Delta n(T) \propto [\mathrm{PL}_{\mathrm{BB}}(T)] \,/\, \left[B(T)^* N_A^-(T))\right]$. The measurement is assumed to be at low injection based on the extrapolated lifetime curves. This assumption is also confirmed using a PC1D simulation [54] of the sample using the maximum observed bulk lifetime of 30 μs, yielding a maximum excess carrier density that is only twice the doping density. This assumption should become even more valid at lower temperatures, as the lifetime decreases with decreasing temperature. For ROI (c), similar to Ref. [55], the measurement cannot be fitted at low temperatures. The reason for that has not been provided in Ref. [55] although it is stated that this type of behavior seems not to be an effect characteristic of dislocation clusters.

The two different extracted values of E_{a} are 75 ± 2.3 meV for ROI (a) and 130 ± 2.9 meV for ROI (c). It may indicate that different impurities occupy these two regions. Compared to ROI (a), ROI (c) shows a stronger reduction of $\mathrm{PL}_{\mathrm{defect}}$ with increasing temperature (Fig. F.10), indicating that recombination strongly decreases with temperature. This suppresses the effect of the temperature dependence of n_i which reduces the magnitude of the decrease of iV_{OC} with increasing temperature. As a result, the temperature sensitivity at ROI (c) is lower.

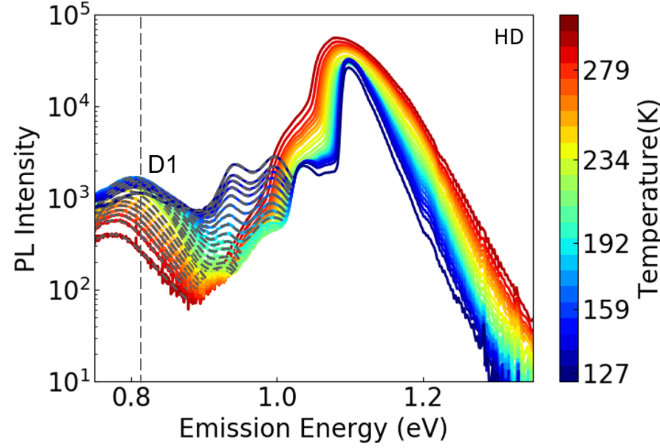

Figure F.9: PL spectra of ROI (c) at a sample temperature range from 127 K to 302 K under 20 Suns.

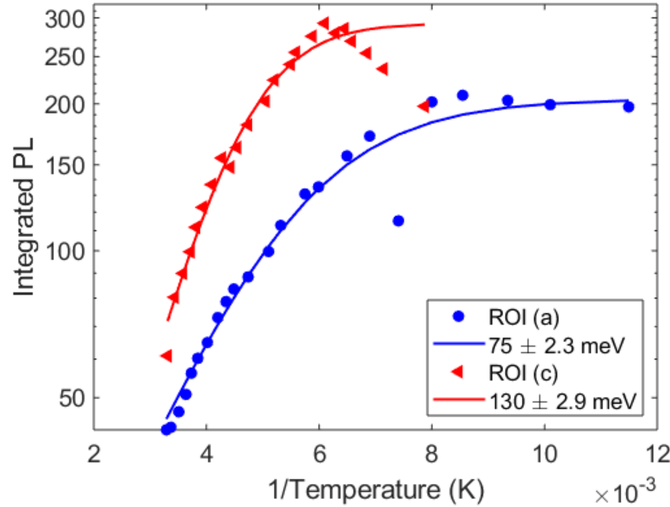

Figure F.10: Arrhenius plot of ROI (a) and (c) with the best fit.

F.IV. Conclusions

We presented a method for measuring temperature dependent iV_{OC} images on metallised and non-metallised samples without the impact of trapping and DRM, by combining PL imaging and QSS-PL front detection measurements. This spatially resolved measurement allows for assessing both local and global temperature characteristics of wafers and cells, providing more information regarding the material properties than conventional global measurements.

The TCs of wafers and cells from different brick heights with different dislocation densities were studied. The local results demonstrate that dislocated areas on wafers show both high and low temperature sensitivity. Moreover, γ is found to exhibit low

values (even negative) in areas of dislocation clusters with low temperature sensitivity.

Global TC(iV_{OC}) values of the investigated wafers and cells are found to be less negative with increasing brick height. Furthermore, the wafers from the top of the bricks show less variability in TC(iV_{OC}) as a function of iV_{OC} compared to the rest of the wafers. This is due to a larger spread of TC(iV_{OC}) which is particularly evident at a medium to low iV_{OC} range observed for the top wafers. This suggests that cells made from wafers from the top of the brick will perform relatively better at higher temperatures. μ-PL was performed at dislocated regions with different TC values. E_a is found to be 130 ± 2.9 meV and 75 ± 2.3 meV for the dislocation clusters with low and high temperature sensitivity, respectively, may indicate that different impurities occupy these two regions thereby resulting in different TC values.

This work highlights the importance of studying TC values with spatial resolution. Future applications of this method could involve optimisation of solar cell and wafer performance under non-STC.

Appendix A

The τ_{eff} images of two wafers originating from the bottom and top of the HD brick at 298 K and 343 K are shown in Figs. F.11 and F.12. Please note these two images correspond with the wafers shown in Fig. F.7.

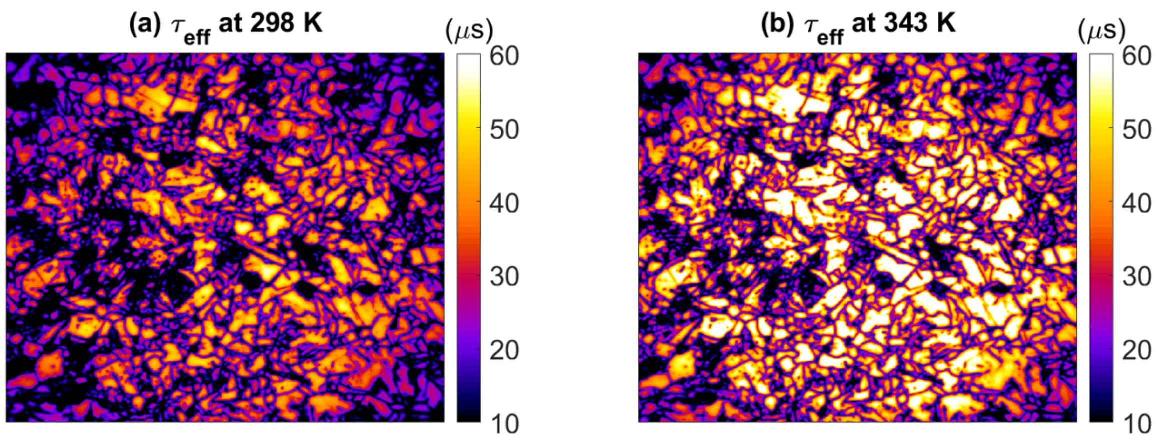

Figure F.11: Spatially resolved τ_{eff} of a wafer from the bottom of the highly dislocated brick under 0.5 Sun illumination at (a) 298 K and (b) 343 K. Note that these images were cropped to present only the regions of interest.

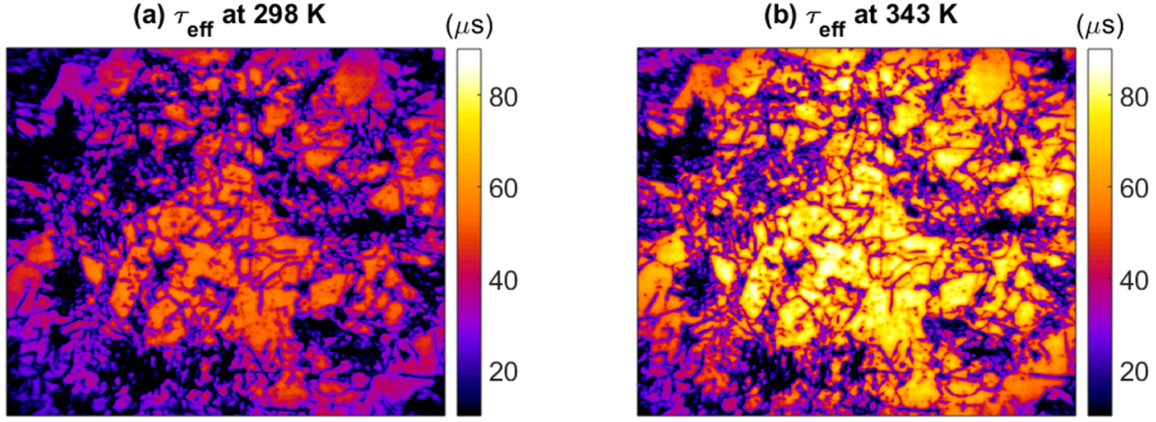

Figure F.12: Spatially resolved τ_{eff} of a wafer from the top of the highly dislocated brick under 0.5 Sun illumination at (a) 298 K and (b) 343 K. Note that these images were cropped to present only the regions of interest.

Appendix B

The activation energy is extracted based on Ref. [52] as the recombination mechanism in this study for the defect PL is donor-acceptor pair recombination [a blue-shift (2-3 meV) of the defect peaks is observed as the light intensity (carrier injection) is increased]. The equation for donor-acceptor pair recombination rate (U_{DAP}) for a p-type semiconductor can be expressed as:

$$U_{\text{DAP}} = \frac{pN_{\text{defect}}C_{p2}t'}{\left(p + p'_{\frac{3}{2}}\right)C_{p2} + t'}, \tag{F.7}$$

where N_{defect} is the defect density, C_{p2} is the capture probability of holes to the acceptors when the donor-acceptor is in the charge state of TWO, t' is the interlevel transition rate between donor and acceptor levels, $p'_{\frac{3}{2}}$ is a carrier density term containing the acceptor energy level and p is the hole concentration.

Assuming $\left(p + p'_{\frac{3}{2}}\right)C_{p2} \gg t'$, Eq. (F.7) can be re-arranged as:

$$U_{\text{DAP}} = \frac{N_{\text{defect}}t'}{\left(1 + \frac{p'_{\frac{3}{2}}}{p}\right)} \tag{F.8}$$

where $p'_{\frac{3}{2}}$ is given by

$$p'_{\frac{3}{2}} = CT^{1.5}e^{-\frac{E_a}{kT}} \tag{F.9}$$

By combing Eqs. (F.8) and (F.9), Eq. (F.6) is obtained and can be used to determine the activation energy.

Acknowledgement

This work was supported by the Australian Government through Australian Renewable Energy Agency [ARENA; project 2017/RND001]. The views expressed herein are not necessarily the views of the Australian Government, and the Australian Government does not accept responsibility for any information or advice contained herein.

Bibliography

[1] "International Technology Roadmap for Photovoltaic (ITRPV): Results 2017," 2018.

[2] "Photovoltaic Devices—Part 1–10, IEC-60904," 2009.

[3] D. Faiman, "Assessing the outdoor operating temperature of photovoltaic modules," *Prog. Photovoltaics*, vol. 16, pp. 307–315, 2008.

[4] M. Green and K. A. Emery, "Silicon solar cells with reduced temperature sensitivity," *Electron. Lett.*, vol. 18, pp. 97–98, 1982.

[5] M. Green, *Solar cells: Operating Principles, Technology, and System Applications.* Prentice-Hall, Englewood Cliffs, 1982.

[6] J. C. C. Fan, "Theoretical temperature dependence of solar cell parameters," *Sol. Cells*, vol. 17, pp. 309–315, 1986.

[7] M. A. Green, "General temperature dependence of solar cell performance and implications for device modelling," *Prog. Photovoltaics Res. Appl.*, vol. 11, pp. 333–340, 2003.

[8] P. Löper, D. Pysch, A. Richter, M. Hermle, S. Janz, M. Zacharias, and S.W. Glunz, "Analysis of the temperature dependence of the open-circuit voltage," *Energy Procedia*, vol. 27, pp. 135–142, 2012.

[9] P. Singh and N. M. Ravindra, "Temperature dependence of solar cell performance — an analysis," *Sol. Energy Mater. Sol. Cells*, vol. 101, pp. 36–45, 2012.

[10] O. Dupré, R. Vaillon, and M. A. Green, "Physics of the temperature coefficients of solar cells," *Sol. Energy Mater. Sol. Cells*, vol. 140, pp. 92–100, 2015.

[11] H. Steinkemper, I. Geisemeyer, M. C. Schubert, W. Warta, and S. W. Glunz, "Temperature-dependent modeling of silicon solar cells-Eg, ni, recombination, and VOC," *IEEE J. Photovoltaics*, vol. 7, pp. 450–457, 2017.

[12] O. Dupré, R. Vaillon, and M. A. Green, *Thermal Behavior of Photovoltaic Devices.* Switzerland: Springer, 2017.

[13] S. M. Sze and K. K. Ng, *Physics of Semiconductor Devices.* New York: John Wiley & Sons, 1981.

[14] O. Dupré, R. Vaillon, and M. A. Green, "Experimental assessment of temperature coefficient theories for silicon solar cells," *IEEE J. Photovoltaics*, vol. 6, pp. 56–60, 2016.

[15] C. Berthod, S. T. Kristensen, R. Strandberg, J. O. Odden, S. Nie, Z. Hameiri, and T. O. Sætre, "Temperature sensitivity of multicrystalline silicon solar cells," *IEEE J. Photovoltaics*, vol. 9, pp. 957–964, 2019.

[16] H. Haug, R. Søndenå, M. S. Wiig, and E. S. Marstein, "Temperature dependent photoluminescence imaging calibrated by photoconductance measurements," *Energy Procedia*, vol. 124, pp. 47–52, 2017.

[17] R. Eberle, S. T. Haag, I. Geisemeyer, M. Padilla, and M. C. Schubert, "Temperature coefficient imaging for silicon solar cells," *IEEE J. Photovoltaics*, vol. 8, pp. 930–936, 2018.

[18] R. Eberle, A. Fell, S. Mägdefessel, F. Schindler, and M. C. Schubert, "Prediction of local temperature-dependent performance of silicon solar cells," *Prog. Photovoltaics Res. Appl.*, vol. 27, pp. 999-1006, 2019.

[19] W. Shockley and W. T. Read, "Statistics of the recombination of holes and electrons," *Phys. Rev.*, vol. 87, pp. 835–842, 1952.

[20] R. N. Hall, "Electron-hole recombination in germanium," *Phys. Rev.*, vol. 87, p. 387, 1952.

[21] B. Mitchell , D. Chung , Q. He, H. Zhang, Z. Xiong, P. P. Altermatt, P. Geelan-Small, and T. Trupke, "PERC solar cell performance predictions from multicrystalline silicon ingot metrology data," *IEEE J. Photovoltaics*, vol. 7, pp. 1619–1626, 2017.

[22] H. Li, F. J. Ma, Z. Hameiri, S. Wenham, and M. Abbott, "On elimination of inactive phosphorus in industrial POCl3 diffused emitters for high efficiency silicon solar cells," *Sol. Energy Mater. Sol. Cells*, vol. 171, pp. 213–221, 2017.

[23] H. Li, F. J. Ma, Z. Hameiri, S. Wenham, and M. Abbott, "An advanced qualitative model regarding the role of oxygen during POCl3 diffusion in silicon," *Phys. Status Solidi - Rapid Res. Lett.*, vol. 11, pp. 1700046-1–4, 2017.

[24] Z. Hameiri, N. Borojevic, L. Mai, N. Nandakumar, K. Kim, and S. Winderbaum, "Low-absorbing and thermally stable industrial silicon nitride films with very low surface recombination," *IEEE J. Photovoltaics*, vol. 7, pp. 996–1003, 2017.

[25] R. Dumbrell, M. K. Juhl, T. Trupke, and Z. Hameiri, "Extracting metal contact recombination parameters from effective lifetime data," *IEEE J. Photovoltaics*, vol. 8, no. 6, pp. 1413–1420, 2018.

[26] R. Dumbrell, M. K. Juhl, T. Trupke, and Z. Hameiri, "Extracting surface saturation current density from lifetime measurements of samples with metallized surfaces," in *7th World Conference on Photovoltaic Energy Conversion*, pp. 3243–3247, 2018.

[27] S. T. Kristensen, S. Nie, M. S. Wiig, H. Haug, R. Strandberg, and Z. Hameiri, "A high-accuracy calibration method for temperature dependent photoluminescence imaging," *9th Int. Conf. Cryst. Silicon Photovoltaics*, pp. 1–6, 2019.

[28] T. Trupke, R. A. Bardos, F. Hudert, P. Wurfel, J. Zhao, A. Wang, and M. A. Green, "Effective excess carrier lifetimes exceeding 100 milliseconds in float zone silicon determined from photoluminescence," in *Proceedings of the 19th European Photovoltaic Solar Energy Conference*, pp. 758–761, 2004.

[29] R. A. Bardosa, T. Trupke, M. C. Schubert, and T. Roth, "Trapping artifacts in quasi-steady-state photoluminescence and photoconductance lifetime measurements on silicon wafers," *Appl. Phys. Lett.*, vol. 88, pp. 053504-1–3, 2006.

[30] T. Trupke and R. A. Bardos, "Photoluminescence: a surprisingly sensitive lifetime technique," *31st IEEE Photovolt. Spec. Conf.*, pp. 903–906, 2005.

[31] T. Trupke and R. A. Bardos, "Self-consistent determination of the generation rate from photoconductance measurements," *Appl. Phys. Lett.*, vol. 85, no. 16, pp. 3611–3613, 2004.

[32] R. A. Bardos and T. Trupke, "Self-consistent determination of the generation rate in photoluminescence and photoconductance lifetime measurements," *31st IEEE Photovolt. Spec. Conf.*, pp. 899–902, 2005.

[33] T. Trupke, M. A. Green, P. Wurfel, P. P. Altermatt, A. Wang, J. Zhao, and R. Corkish, "Temperature dependence of the radiative recombination coefficient of intrinsic crystalline silicon," *J. Appl. Phys.*, vol. 94, pp. 4930–4937, 2003.

[34] P. P. Altermatt, F. Geelhaar, T. Trupke, X. Dai, A. Neisser, and E. Daub, "Injection dependence of spontaneous radiative recombination in c-Si: experiment, theoretical analysis, and simulation," *Proc. 5th Conf. Numer. Simul. Optoelectron. Devices*, pp. 47–48, 2005.

[35] R. Pässler, "Dispersion-related description of temperature dependencies of band gaps in semiconductors," *Phys. Rev. B*, vol. 66, pp. 085201-1–18, 2002.

[36] R. Couderc, M. Amara, and M. Lemiti, "Reassessment of the intrinsic carrier density temperature dependence in crystalline silicon," *J. Appl. Phys.*, vol. 115, pp. 093705-1–5, 2014.

[37] S. T. Kristensen, S. Nie, C. Berthod, R. Strandberg, J. O. Odden, and Z. Hameiri, "How gettering affects the temperature densitivity of the implied open circuit voltage of multicrystalline silicon wafers," *46th IEEE Photovoltaic Specialists Conference*, pp. 1–7, 2019.

[38] M. A. Green, "Radiative efficiency of state-of-the-art photovoltaic cells," *Prog. Photovoltaics*, vol. 20, pp. 472–476, 2012.

[39] C. Berthod, R. Strandberg, J. O. Odden, and T. O. Sætre, "Reduced temperature sensitivity of multicrystalline silicon solar cells with low ingot resistivity," *43rd IEEE Photovolt. Spec. Conf.*, pp. 2398–2402, 2016.

[40] C. Berthod, R. Strandberg, and J. O. Odden, "Temperature coefficients of compensated silicon solar cells - influence of ingot position and blend-in-ratio," *Energy Procedia*, vol. 77, pp. 15–20, 2015.

[41] H. Haug, C. Berthod, Å. Skomedal, J. O. Odden, S. E. Marstein, and R. Søndenå, "Simulated and measured temperature coefficients in compensated silicon wafers and solar cells," *Sol. Energy Mater. Sol. Cells*, vol. 200, pp. 1–8, 2019.

[42] R. A. Sinton, "Predicting multi-crystalline solar cell efficiency from life-time measured during cell fabrication," *3rd World Conf. Photovolt. Energy Convers.*, pp. 1028–1031, 2003.

[43] J. Isenberg, J. Dicker, and W. Warta, "Averaging of laterally inhomogeneous lifetimes for one-dimensional modeling of solar cells," *J. Appl. Phys.*, vol. 94, pp. 4122–4130, 2003.

[44] D. Macdonald, A. Cuevas, A. Kinomura, Y. Nakano, and L. J. Geerligs, "Transition-metal profiles in a multicrystalline silicon ingot," *J. Appl. Phys.*, vol. 97, pp. 033523-1–7, 2005.

[45] H. C. Sio, S. P. Phang, P. Zheng, Q. Wang, W. Chen, H. Jin, and D. Macdonald, "Recombination sources in p-type high performance multicrystalline silicon," *Jpn. J. Appl. Phys.*, vol. 56, p. 08MB16-1-16, 2017.

[46] R. M. R. Lee Chin, Y. Zhu, G. Coletti, S. Binetti, M. Pollard, and Z. Hameiri, "Insights into bulk defects in n-type monocrystalline silicon wafers via temperature-dependent micro-photoluminescence spectroscopy," *7th World Conf. Photovolt. Energy Conversion*, pp. 2524–2527, 2018.

[47] D. Macdonald, A. Liu, H. T. Nguyen, S. Y. Lim, and F. E. Rougieux, "Physical modelling of luminescence spectra from crystalline silicon," *31st Eur. Photovolt. Sol. Energy Conf. Exhib. Phys.*, pp. 440–443, 2015.

[48] N. A. Drozdov, A. A. Patrin, and V. D. Tkachev, "Recombination radiation on dislocations in silicon," *Sov. Phys.–JETP Lett*, vol. 23, pp. 597–599, 1976.

[49] J. F. Kielkopf, "New approximation to the Voigt function with applications to spectral-line profile analysis," *J. Opt. Soc. Am.*, vol. 63, pp. 987–995, 1973.

[50] Y. Yang, J. Bao, C. Wang, and M. J. Aziz, "Sub-bandgap luminescence centers in silicon created by self-ion implantation and thermal annealing," *J. Appl. Phys.*, vol. 107, pp. 123109-1–5, 2010.

[51] M. Kittler and M. Reiche, "Structure and properties of dislocations in silicon," in *Structure and Properties of Dislocations in Silicon, Crystalline Silicon - Properties and Uses*, P. S. Basu, Ed. InTech, 2011, p. 66.

[52] L. W. Aukerman and M. F. Millea, "Steady-state recombination via donor-acceptor pairs," *Phys. Rev.*, vol. 148, pp. 759–765, 1966.

[53] P. P. Altermatt, A. Schenk, B. Schmithüsen, and G. Heiser, "A simulation model for the density of states and for incomplete ionization in crystalline silicon. II. Investigation of Si:As and Si:B and usage in device simulation," *J. Appl. Phys.*, vol. 100, pp. 113715-1–7, 2006.

[54] D. A. Clugston and P. A. Basore, "PC1D version 5: 32-bit solar cell modeling on personal computers," *26th IEEE Photovolt. Spec. Conf.*, pp. 207–210, 1997.

[55] M. Suezawa, Y. Sasaki, and K. Sumino, "Dependence of photoluminescence on temperature in dislocated silicon crystals," *Phys. Status Solidi*, vol. 79, pp. 173–181, 1983.